

Gaia DR2 Proper Motions of Dwarf Galaxies within 420 kpc:

Orbits, Milky Way Mass, Tidal Influences, Planar Alignments, and Group Infall

T. K. Fritz^{1,2}, G. Battaglia^{1,2}, M. S. Pawlowski^{3*}, N. Kallivayalil⁴, R. van der Marel^{5,6}, S. T. Sohn⁵, C. Brook^{1,2}, and G. Besla⁷

¹ Instituto de Astrofísica de Canarias, calle Via Lactea s/n, E-38205 La Laguna, Tenerife, Spain
e-mail: tfritz@iac.es

² Universidad de La Laguna, Dpto. Astrofísica, E-38206 La Laguna, Tenerife, Spain

³ Department of Physics and Astronomy, University of California, Irvine, CA 92697, USA

⁴ Department of Astronomy, University of Virginia, Charlottesville, 530 McCormick Road, VA 22904-4325, USA

⁵ Space Telescope Science Institute, 3700 San Martin Drive, Baltimore, MD 21218, USA

⁶ Center for Astrophysical Sciences, Department of Physics & Astronomy, Johns Hopkins University, Baltimore, MD 21218, USA

⁷ Steward Observatory, University of Arizona, 933 North Cherry Avenue, Tucson, AZ 85721, USA

ABSTRACT

A proper understanding of the Milky Way (MW) dwarf galaxies in a cosmological context requires knowledge of their 3D velocities and orbits. However, proper motion (PM) measurements have generally been of limited accuracy and available only for more massive dwarfs. We therefore present a new study of the kinematics of the MW dwarf galaxies. We use the Gaia DR2 for those dwarfs that have membership information available from literature spectroscopy. We derive the PMs for 39 galaxies out to 420 kpc, and generally find good consistency for the subset with measurements available from other studies. We derive the implied Galactocentric velocities, and calculate orbits in canonical MW halo potentials of "low" ($0.8 \times 10^{12} M_{\odot}$) and "high" mass ($1.6 \times 10^{12} M_{\odot}$). Comparison of the distributions of orbital apocenters and 3D velocities to the halo virial radius and escape velocity, respectively, suggests that the satellite kinematics are best explained in the high-mass halo. Tuc III, Segue 2, Crater II, and additional candidates have orbital pericenters small enough to imply significant tidal influences. Relevant to the missing satellite problem, the fact that fewer galaxies are observed to be near apocenter than near pericenter implies that there must be a population of distant dwarf galaxies yet to be discovered. Of the 39 dwarfs: 12 have orbital poles that do not align with the MW plane of satellites (given reasonable assumptions about its intrinsic thickness); 11 have insufficient PM accuracy to establish whether they align; and 16 satellites align, of which 11 are co-orbiting and (somewhat surprisingly, in view of prior knowledge) 5 are counter-orbiting. Group infall might have contributed to this, but no definitive association is found for the members of the Crater-Leo group.

Key words. Astrometry - Proper motions - Galaxies: dwarf - Galaxies: kinematics and dynamics - Local Group - Galaxies: evolution

1. Introduction

The determination of the orbital properties of the dwarf galaxies surrounding the Milky Way (MW) is a crucial step for unraveling the formation and evolutionary paths of these galaxies: did the dwarf spheroidals (dSphs) and ultra-faint dwarfs (UFDs) lose their gas due to internal stellar feedback or due to a combination of internal and external effects, such as UV-background heating and/or tidal and ram-pressure stripping from the large Local Group spirals (e.g. Mayer et al. 2006; Revaz & Jablonka 2018, Bermejo-Climent et al. in prep.)? Are the metallicity gradients observed for several of the Milky Way "classical" dwarf spheroidal galaxies (e.g. Tolstoy et al. 2004; Battaglia et al. 2006, 2011) an intrinsic property of these systems or could interactions with the Milky Way have had a role in setting their presence or erasing them in some cases (Sales et al. 2010)?

From a theoretical perspective, depending on the orbital and internal characteristics of the object (e.g. in terms of the mass density profile of its dark matter halo) it has been argued that such interactions could potentially transform initially

discy/rotating dwarfs in spheroidal/pressure-supported systems (e.g. Mayer et al. (2001, 2006); Kazantzidis et al. (2017); however, the existence of very isolated dwarf galaxies, or those likely on their first approach towards the MW, having a spheroidal morphology and being in the process of losing/exhausting their gas would suggest otherwise (e.g. VV 124, Leo T, Phoenix I). Nonetheless, signs of tidal disturbance have been detected in the spatial distribution of the stellar component of some classical dwarf galaxies and ultra-faint systems (e.g. Carina I, Hercules I, Boötes I, see e.g. Battaglia et al. 2012; Roderick et al. 2015, 2016) and it is still debated whether the presence of tidally unbound stars in spectroscopic samples can alter inferences of the dark matter (DM) distribution in these galaxies obtained from the observed line-of-sight velocity dispersion, in particular in the outer parts (e.g. Łokas et al. 2008; Łokas 2009).

Other interesting aspects that the orbital properties allow to explore are whether some of the MW satellites were accreted to the MW as part of a group of dwarf galaxies as suggested for example by the discovery of possible satellites of the LMC (Koposov et al. 2015a; Bechtol et al. 2015) as well as if they are preferentially distributed on a planar structure (Pawlowski et al. 2012).

* Hubble fellow

These are only a few of the questions that can potentially be addressed by knowledge of the orbital properties of the MW dwarf galaxies. The very first step towards this goal is the determination of the 3D bulk motion of these systems. While determinations of the systemic heliocentric radial velocity are available in the literature for all of the MW classical dwarf spheroidal galaxies and most of the ultra-faint systems discovered so far, astrometric proper motions have become available for the full set of MW classical dwarf spheroidals only very recently and no astrometric proper motion had been available for any of the ultra-faint dwarf galaxies, apart from Segue 1 (Fritz et al. 2017b).

The second release of data from the Gaia mission (Gaia Collaboration et al. 2018a) has started a revolution in this respect. Gaia Collaboration et al. (2018b) demonstrated the power of the Gaia DR2 data for the study of the kinematics of stellar systems around the Milky Way using 75 globular clusters, the Magellanic Clouds, the 9 classical MW dwarf spheroidal galaxies and the Boötes I UFD. In several cases the precisions are exquisite, in others they are comparable to what can be achieved with HST, but with the clear advantage of being in an absolute reference frame.

Gaia DR2 has opened the door as well to the determinations of the systemic proper motion of dozens of the other dwarf galaxies surrounding the Milky Way. In this work, we obtain systemic proper motions for most of the systems within 420 kpc from the MW. The paper is structured as follows: in Sect. 2 we describe the data-sets used for the analysis and in Sect. 3 the methodology adopted to determine systemic proper motions; Sect. 4 presents the determination of space velocities and orbital properties of the objects in the sample; we discuss the main results in Sect. 5 and present conclusions and summary in Sect. 6.

2. Data

Our sample of galaxies consists of the vast majority of galaxies and galaxy candidates within 420 kpc of the Milky Way. We omitted: the Magellanic Clouds, because they have already well established motions and their measurable internal motions complicate measurements; Leo T, due to its low luminosity combined to its large distance; and Boötes III, due to its unclear nature as a galaxy or stream (Grillmair 2009). We were inclusive of objects whose nature as globular cluster or as dwarf galaxy is still under debate, such as for example Crater I (Kirby et al. 2015; Voggel et al. 2016).

Our work is mainly based on the *Gaia* (Gaia Collaboration et al. 2016) data release 2 (GDR2) (Gaia Collaboration et al. 2018a). Furthermore, we use literature spectroscopic data sets of dwarf galaxies to ease identification of members. For most galaxies we use the catalogs shown in Table 1.¹ For the Sagittarius dSph we use APOGEE DR14 data (Majewski et al. 2017), selecting all the stars within 30' of the nominal center. We also drop from the sample Pegasus III because of the lack of Gaia DR2 matches for the spectroscopic members in Kim et al. (2016).

Because we rely on spectroscopic data some satellites are omitted from our sample. Most of those are so faint and/or distant (like for example Indus II) that calculations show that no member stars are expected above the *Gaia* DR2 magnitude limit.

¹ We note that it appears that the long electronic Tab. 1 of Walker et al. (2016) is wrong for Grus I: it disagrees with Tab. 1 in the pdf version of that paper for the members, with the members in the electronic table showing a large v_{helio} dispersion. We here use only the members of Tab. 3 in Walker et al. (2016).

Others, like Sagittarius II and Pictoris II, are in principle bright enough, but no spectroscopic data-set has been published yet.

3. Proper motions

3.1. Method

Except for a couple of cases, we use only stars for which membership probabilities (be it a binary probability or not) are available as based on literature spectroscopic studies. For those cases when membership probabilities were not provided in the source paper, we calculate them ourselves (see notes in Tab. 1) using the heliocentric v_{helio} and, when provided, also $\log(g)$: essentially we assign probabilities based on the likelihood of star to be a giant and have a velocity similar to the systemic velocity of the galaxy.

The selection of probable members is later refined by including information from Gaia DR2. We first check whether stars with spectroscopic information have a match within 1" in Gaia DR2 that also has Gaia DR2 kinematic information. We then require at least 40% membership probability according to the spectroscopic analysis, as well as requiring the stars to have a parallax deviating less than 2σ from the value expected given the distance to the galaxy, and tangential velocities (in the right ascension and declination direction) less than 2σ from an approximation of the escape speed at the distance of the object. Our estimate of the local escape speed corresponds approximately to that expected for a Navarro, Frenk and White (NFW) dark matter (DM) halo (Navarro et al. 1996) with virial mass $1.2 \times 10^{12} M_{\odot}$. After converting the escape speed to mas/yr at the distance of the object, we also add the expected 'proper motion' due to the reflex motion of the Sun given the position and distance of the satellite. The escape speed criteria is applied in both dimensions (right ascension and declination) separately. All these criteria are relatively inclusive, but, because we use several of them, the sample is still expected to be rather clean. Finally, we apply an outlier rejection criteria, excluding those stars whose proper motion deviates by more than 3σ in at least one proper motion dimension. Overall not many stars are excluded from the initial samples, see Table 1, especially for the fainter galaxies.

A few objects have only two likely members with kinematic information in Gaia DR2 and passing our criteria (see Table 1). The final step of outlier rejection cannot therefore be applied on these samples containing only two stars. We inspected the motions of these cases with greater care; most of them agree well with each other, and we use them in the following w/o distinction. In the case of Hydrus I the motions of the two currently public likely members do not agree with each other. In this case we compared the motions with the other GDR2 stars within 1.5 half light radii. A clear clump is visible around the proper motion of the brightest of the two stars: from this we conclude that the brighter stars in Koposov et al. (2018) is a member while the fainter star is not. Here we use the motion of the brighter member. Also for the other galaxies with few members we checked whether Gaia DR2 stars within the half-light radius of these systems, but without spectroscopic measurements, clump close to the member stars in proper motion space. For simplicity we omitted to add these others stars to our sample.

After we have selected which stars are members, we calculate the average proper motion of the object in right ascension (μ_{α^*}) and declination (μ_{δ}) and the average correlation coefficient between μ_{α^*} and μ_{δ} by taking an error weighted average of all the member stars. These values are given in Table 2. For the conversion to velocities and for our analysis we also add to the proper motions errors in both dimensions a systematic error of

Table 1. Sample of objects. Column 1 lists the object name; col. 2 the number of spectroscopic members; col. 3 gives the number of spectroscopic members that have a match within 1" in Gaia DR2 and col. 4 is as before but which have kinematic information in Gaia DR2; col. 5 lists the number of spectroscopic members that passed our additional membership criteria (see text); in col.6 we provide the source of the spectroscopic catalogs. In the last column we mark with y, when we derived the spectral membership probability ourselves

name	spec members	in Gaia	kinematic	final sample	source
Aquarius II	9	2	2	2	1
Bootes I	78	45	38	38	2, 30
Bootes II	5	4	4	4	3
CanVen I	237	69	57	57	2, 4
CanVen II	25	13	11	11	4
Carina I	780	772	693	693	5
Carina II	18	18	18	18	6
Carina III	4	4	4	4	6
Coma Berenices I	59	18	18	17	4
Crater I	36	10	10	10	7, 8
Crater II	59	59	58	58	9, Y
Draco I	496	495	440	436	10, Y
Draco II	9	6	6	6	11
Eridanus II	28	13	12	12	12
Fornax I	2918	2903	2549	2529	5, 13
Grus I	7	5	5	5	14
Hercules I	17	5	4	4	4, 15
Horologium I	5	5	4	4	16
Hydra II	13	6	6	6	7
Leo I	328	299	241	241	17
Leo II	175	111	103	103	18
Leo IV	18	5	3	3	4
Leo V	8	5	5	5	19
Phoenix I	194	83	71	71	20
Pisces II	7	2	2	2	7
Reticulum II	28	28	27	27	21
Sagittarius I	151	151	124	96	APOGEE, Y
Sculptor I	1775	1764	1491	1472	5, 13
Segue 1	71	15	14	13	22
Segue 2	13	2	2	2	23
Sextans I	549	392	328	325	24
Triangulum II	13	6	5	5	25
Tucana II	37	29	29	29	14
Tucana III	50	42	40	38	26, 27
Ursa Major I	40	29	23	23	2, 4
Ursa Major II	28	17	15	15	2, 4
Ursa Minor I	212	152	137	137	28
Willman 1	14	8	7	7	2
Hydrus I	2	2	2	1	29

References. (1) Torrealba et al. (2016b); (2) Martin et al. (2007); (3) Koch et al. (2009); (4) Simon & Geha (2007); (5) Walker et al. (2009b); (6) Li et al. (2018b); (7) Kirby et al. (2015); (8) Voggel et al. (2016); (9) Caldwell et al. (2017); (10) Walker et al. (2015); (11) Martin et al. (2016); (12) Li et al. (2017); (13) Battaglia & Starkenburg (2012, and references therein); (14) Walker et al. (2016); (15) Adén et al. (2009); (16) Koposov et al. (2015b); (17) Mateo et al. (2008); (18) Spencer et al. (2017); (19) Walker et al. (2009a); (20) Kacharov et al. (2017); (21) Simon et al. (2015); (22) Simon et al. (2011); (23) Kirby et al. (2013); (24) Cicuéndez et al. (2018); (25) Kirby et al. (2017); (26) Simon et al. (2017); (27) Li et al. (2018a); (28) Kirby et al. (2010); (29) Koposov et al. (2018); (30) Koposov et al. (2011).

0.035 mas/yr (see Gaia Collaboration et al. (2018b)), which we assume to be uncorrelated between α and δ .

The obtained proper motions are of high quality as shown by the comparison with independent measurements (see Sect. 3.2) and by the reduced χ^2 distribution between individual proper motion measurements and sample averages, which follows what is expected for samples of the sizes considered here. As mentioned above, in the cases for which only an handful of spectroscopic members are available we have double checked that the proper motion of Gaia DR2 stars within 1.5 half-light radii of

the object center share a similar proper motion to that estimated from the spectroscopic members. Note that while in the inner halo there are still many halo stars in streams and in the smooth halo component, we expect the contamination from halo stars to be much lower at large Galactocentric distances. Thus the motions of distant satellites will be more reliable in that respect.

3.2. Comparison with other measurements

Gaia DR2 proper motions are known to have systematic uncertainties of the order 0.035 mas/yr (Gaia Collaboration et al. 2018b). Since some of the closer galaxies in our sample have measurement uncertainties smaller or comparable to this, it is important to compare our Gaia DR2 proper motions with those measured using independent instruments and methods. Gaia Collaboration et al. (2018b) compared their Gaia DR2 proper motion measurements of 9 classical dSphs with those reported in the literature. They found that in general, the Gaia DR2 measurements are consistent with previous measurements (based on ground-based and HST data) at 2σ level. Moreover, when compared to only HST-based measurements, the agreement becomes even better, especially when systematic uncertainties are considered. Our proper motions presented in Table 2 are consistent with the results by Gaia Collaboration et al. (2018b) within the quoted 1σ uncertainties for 6 out of the 9 classical dSphs. Among the 3 other dSphs, our measurements for Fornax I and Sextans I agree with those of Gaia Collaboration et al. (2018b) at 2σ level. For Sagittarius I, we find that the two measurements are discrepant by 0.044 mas/yr in the μ_α direction (while consistent in the μ_δ direction). These discrepancies are due to the different samples of stars used for deriving the proper motions, and this is pronounced when we average stars from a wide angular area such as Sagittarius I. Nevertheless, our results for classical dSphs are generally in good agreement with Gaia Collaboration et al. (2018b), so we are able to make the same assessments as in their paper.

In addition to the 9 classical dSphs, the proper motion of Segue 1 was recently measured by Fritz et al. (2017b) using SDSS and LBC: $(\mu_{\alpha^*}, \mu_\delta) = (-0.37 \pm 0.57, -3.39 \pm 0.58)$ mas/yr. The Gaia DR2-based proper motion agree with this measurement at the $\sim 2\sigma$ level in the right ascension, and $< 1\sigma$ level in the declination, similar to what is found for classical dSphs. All in all, we conclude that our proper motions using Gaia DR2 are generally consistent with measurements made independently using other instruments.

At the time of writing, Simon (2018) derived Gaia DR2 based proper motions for UFDs within 100 kpc from the Milky Way, also based on catalogs of spectroscopic member stars from the literature: for the objects in common, there is excellent (within 1σ) agreement with our determinations, except for Segue 2 and Tuc III, for which there is a 2σ difference; the agreement between ours and Simon's independent determinations of proper motions for UFDs, which do differ in the details of the methodology, lends support to the robustness of the results. In the case of Tuc III, the differences are likely resulting from the fact that we include stars in the stream (Li et al. 2018a) when deriving proper motions. The case of Segue 2 is objectively a particularly difficult one, as only 2 spectroscopic member stars are used and Gaia DR2 stars within 1.5 half-light radius do not cluster tightly around the value of the spectroscopic members.

4. Velocities and orbital parameters

In order to convert the measured proper motion into tangential velocity in an heliocentric reference frame, we adopted the heliocentric distances by McConnachie (2012) or, if the object was discovered posterior to 2012, we adopted the distances in the object discovery paper. For the error budget on the heliocentric tangential velocity, we included the published errors in the object's distance modulus, and, to be conservative, added in quadrature an error floor of 0.1 mag. Table 2 lists the 3D Galactocentric

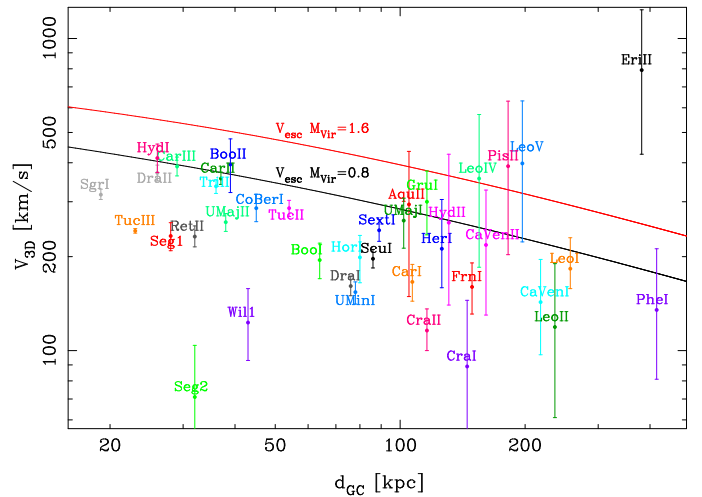


Fig. 1. Total velocity of all galaxies in the sample (points with errorbars). The curves show the escape velocity for the two potentials used in this paper, i.e. *MWPotential14* with a NFW halo of virial mass $0.8 \times 10^{12} M_\odot$ (black line) and a more massive variant, with virial mass $1.6 \times 10^{12} M_\odot$ (red line).

velocities, and the Galactocentric radial and tangential velocity components; these were derived assuming a 8.2 ± 0.1 kpc distance of the Sun from the Milky Way center and a velocity of the Sun with respect to the Milky Way center of $(11, 248, 7.3)$ km/s (with errors $(1, 3, 0.5)$ km/s) in a reference frame in which the x-axis is positive pointing inwards from the Sun to the Galactic center, the y-axis in the direction of Galactic rotation and the z-axis towards the North Galactic Cap (Bland-Hawthorn & Gerhard 2016). We run 2000 Monte Carlo simulations drawing μ_{α^*} , μ_δ and the heliocentric radial velocities randomly, from Gaussian distributions centered on the measured values and dispersions given by the respective errors. When extracting random values for μ_δ we do consider the correlation between the μ_{α^*} and μ_δ , listed in Table 2. The randomly simulated kinematic properties are then transformed into velocities in a Cartesian heliocentric (and then Galactocentric) reference system. In the tables and figures we do not use the median of the Monte Carlo simulations as the most likely value, but the values obtained directly from the measurements, because the median of the Monte Carlo simulations is biased for positive definite values when the errors are close to being as large or larger than the expected values. The asymmetric error bars come from the 1σ distribution of values from the Monte Carlo simulations, similar as in Fritz et al. (2017b). Precisely, we scale the error bars by multiplying with the most likely value and dividing by the median value of the distribution from the Monte Carlo simulations. In this way we avoid that the errors rescaling leads to the inclusion of unphysical parameters into the error bars. From the Galactocentric velocities we also derive estimates of the orbital poles. We show the total velocities of all galaxies in Figure 1.

We then use the publicly available code *galpy* to integrate orbits in a Galactic potential. We adopt the standard *MWPotential14* model, which has three components: a spherical bulge, a disc and a NFW halo (see Bovy et al. 2015 for details). For the MW dark matter halo mass we explore two cases: a light halo with virial mass $0.8 \times 10^{12} M_\odot$ (Bovy 2015) and an heavier model, identical to *MWPotential14* but for the MW DM halo virial mass, which is $1.6 \times 10^{12} M_\odot$ (Fritz et al. 2017a). In Table 3 we lists the apocenter, pericenter and eccentricity values derived with these two potentials. The eccentricity is calculated

Table 2. Distance and kinematic properties of objects in our sample. Column 1 lists the object name, col. 2 its Galactocentric distance, col.3 and 4 give the measured proper motion, col. 5 the correlation coefficient between them, col. 6 the 3D Galactocentric velocity; col.6 the Galactocentric V_{rad} ; col. 7 the Galactocentric V_{tan} . Note that no systematics is included in the estimates of the proper motions listed in this table (see main text). We warn the reader that, since in some cases the errors are large and due to the existing correlation between the two proper motion directions, for detailed calculations it is best to start from the measured quantities (i.e. the proper motions).

satellite	$d_{\text{GC}}[\text{kpc}]$	$\mu_{\alpha^*}[\text{mas/yr}]$	$\mu_{\delta}[\text{mas/yr}]$	$C_{\mu_{\alpha^*}\mu_{\delta}}$	$V_{3\text{D}}[\text{km/s}]$	$V_{\text{rad}}[\text{km/s}]$	$V_{\text{tan}}[\text{km/s}]$
Aqu II	105	-0.252 ± 0.527	0.011 ± 0.448	0.131	294^{+141}_{-145}	43^{+20}_{-21}	291^{+141}_{-146}
Boo I	64	-0.554 ± 0.092	-1.111 ± 0.068	0.163	195^{+26}_{-25}	95^{+4}_{-4}	170^{+30}_{-29}
Boo II	39	-2.686 ± 0.389	-0.53 ± 0.287	-0.186	395^{+82}_{-74}	-48^{+15}_{-16}	392^{+84}_{-77}
CanVen I	218	-0.159 ± 0.094	-0.067 ± 0.054	0.105	143^{+53}_{-46}	84^{+4}_{-3}	116^{+53}_{-51}
CanVen II	161	-0.342 ± 0.232	-0.473 ± 0.169	-0.006	218^{+109}_{-88}	-93^{+8}_{-8}	197^{+109}_{-94}
Car I	107	0.485 ± 0.018	0.132 ± 0.016	0.084	166^{+23}_{-22}	1^{+3}_{-3}	166^{+23}_{-22}
Car II	37	1.867 ± 0.078	0.082 ± 0.072	-0.008	356^{+17}_{-15}	204^{+5}_{-5}	292^{+21}_{-19}
Car III	29	3.046 ± 0.12	1.565 ± 0.135	0.066	389^{+28}_{-26}	46^{+6}_{-7}	386^{+28}_{-26}
ComBer I	45	0.471 ± 0.109	-1.716 ± 0.104	-0.427	286^{+31}_{-27}	29^{+5}_{-5}	284^{+31}_{-28}
Cra I	145	-0.045 ± 0.28	-0.165 ± 0.172	-0.185	89^{+56}_{-46}	-13^{+11}_{-11}	88^{+55}_{-46}
Cra II	116	-0.184 ± 0.061	-0.106 ± 0.032	-0.041	116^{+20}_{-16}	-84^{+4}_{-4}	80^{+24}_{-23}
Dra I	76	-0.013 ± 0.013	-0.158 ± 0.015	0.131	161^{+12}_{-11}	-88^{+3}_{-3}	134^{+14}_{-13}
Dra II	26	1.242 ± 0.276	0.845 ± 0.285	-0.591	371^{+22}_{-21}	-156^{+12}_{-12}	336^{+23}_{-22}
Eri II	382	0.159 ± 0.292	0.372 ± 0.34	-0.257	792^{+444}_{-366}	-61^{+12}_{-12}	790^{+445}_{-368}
Frn I	149	0.375 ± 0.004	-0.401 ± 0.005	-0.46	160^{+31}_{-29}	-41^{+2}_{-2}	154^{+31}_{-30}
Gru I	116	-0.256 ± 0.173	-0.447 ± 0.241	0.246	300^{+76}_{-65}	-203^{+7}_{-7}	221^{+82}_{-79}
Her I	126	-0.434 ± 0.214	-0.401 ± 0.168	0.085	212^{+93}_{-53}	151^{+5}_{-5}	149^{+98}_{-72}
Hor I	80	0.891 ± 0.088	-0.55 ± 0.08	0.294	199^{+35}_{-34}	-34^{+5}_{-5}	196^{+35}_{-35}
Hyd II	131	-0.416 ± 0.519	0.134 ± 0.422	-0.427	257^{+169}_{-117}	129^{+22}_{-21}	223^{+157}_{-113}
Leo I	257	-0.086 ± 0.059	-0.128 ± 0.062	-0.358	183^{+47}_{-25}	168^{+3}_{-3}	73^{+49}_{-37}
Leo II	236	0.02 ± 0.09	-0.201 ± 0.093	-0.289	119^{+71}_{-58}	16^{+4}_{-4}	118^{+71}_{-58}
Leo IV	155	-0.59 ± 0.531	-0.449 ± 0.358	-0.237	356^{+215}_{-171}	13^{+20}_{-20}	355^{+215}_{-170}
Leo V	197	-0.097 ± 0.557	-0.628 ± 0.302	0.047	398^{+233}_{-175}	42^{+19}_{-20}	396^{+234}_{-175}
Phe I	415	0.079 ± 0.099	-0.049 ± 0.12	-0.162	135^{+54}_{-54}	-116^{+4}_{-4}	68^{+44}_{-35}
Pis II	182	-0.108 ± 0.645	-0.586 ± 0.498	0.053	390^{+240}_{-187}	-79^{+24}_{-24}	382^{+236}_{-185}
Ret II	32	2.398 ± 0.04	-1.319 ± 0.048	0.166	232^{+17}_{-17}	-102^{+3}_{-3}	208^{+19}_{-19}
Sgr I	19	-2.736 ± 0.009	-1.357 ± 0.008	0.114	316^{+13}_{-11}	141^{+2}_{-2}	283^{+13}_{-13}
Scu I	86	0.085 ± 0.006	-0.133 ± 0.006	0.157	197^{+14}_{-13}	75^{+1}_{-2}	182^{+13}_{-14}
Seg 1	28	-1.698 ± 0.195	-3.501 ± 0.175	-0.087	233^{+24}_{-24}	116^{+6}_{-6}	202^{+28}_{-27}
Seg 2	32	1.33 ± 0.51	-0.891 ± 0.39	0.147	71^{+35}_{-23}	51^{+12}_{-13}	49^{+30}_{-24}
Sext I	89	-0.438 ± 0.028	0.055 ± 0.028	-0.238	243^{+20}_{-19}	79^{+2}_{-3}	230^{+21}_{-19}
Tri II	36	0.588 ± 0.187	0.554 ± 0.162	0.032	336^{+17}_{-17}	-255^{+5}_{-5}	218^{+25}_{-26}
Tuc II	54	0.916 ± 0.042	-1.169 ± 0.053	-0.375	286^{+17}_{-17}	-187^{+4}_{-4}	216^{+23}_{-23}
Tuc III	23	-0.117 ± 0.036	-1.701 ± 0.036	-0.393	242^{+4}_{-4}	-232^{+3}_{-3}	66^{+6}_{-6}
U Maj I	102	-0.683 ± 0.094	-0.72 ± 0.13	-0.1	261^{+47}_{-48}	11^{+4}_{-3}	261^{+47}_{-48}
U Maj II	38	1.691 ± 0.053	-1.903 ± 0.066	-0.115	258^{+17}_{-17}	-59^{+3}_{-3}	251^{+18}_{-17}
U Min I	78	-0.184 ± 0.026	0.082 ± 0.023	-0.387	154^{+12}_{-13}	-71^{+3}_{-3}	137^{+14}_{-14}
Wil 1	43	0.199 ± 0.187	-1.342 ± 0.366	-0.154	123^{+35}_{-30}	18^{+6}_{-7}	122^{+35}_{-31}
Hyd I	26	4.044 ± 0.312	-1.755 ± 0.276	0.22	414^{+45}_{-42}	-53^{+13}_{-13}	411^{+45}_{-43}

as $ecc = (r_a - r_p)/(r_a + r_p)$ within *galpy*. The central value in the table can be slightly different due to rounding, and the errors are often changed due to our rescaling. We note that the distance of the Sun to the Galactic center and the Sun motion are slightly different than what used above, but in previous works it was found that this was causing only minor changes to the orbital properties; in our case, the observational sources of errors are going to be dominant in most cases. We run 500 Monte Carlo simulations for the orbit integrations.

5. Discussion

Figure 2 shows the orbital properties of the objects in the sample, quantified as the pericenter versus apocenter (for the heavy and light NFW halo in the top and bottom panel, respectively). We only plot objects with an error in 3D velocity approximately less than 100 km/s. That way we are less biased towards large values, as it would be the case for positive definite properties with large errors. In Fig. 3 we plot an all-sky view of the orbital poles of the objects in the sample, concentrating on those within 200kpc, and comparing their location on this plane with the vast polar structure (VPOS) of satellites (Pawlowski et al. 2012). Several considerations can be made from these figures.

Table 3. Orbital properties of objects in our sample. Column 1 lists the object name, col. 2, 3 and 4 the pericenter, apocenter and eccentricities of the orbit around the Milky Way in the more massive potential of the DM halo with virial mass $1.6 \times 10^{12} M_{\odot}$, col. 5, 6 and 7 show the same properties, derived in the less massive potential of $0.8 \times 10^{12} M_{\odot}$ (see main text). Note that several objects have apocenter distances larger than the Local Group extent; these should be taken with a grain of salt, as e.g. our estimates do not include the effect of the gravitational potential of M 31, and should be seen as indication that the given object is on its first infall to the Milky Way.

satellite	peri(1.6)[kpc]	apo(1.6)[kpc]	ecc(1.6)[kpc]	peri(0.8)[kpc]	apo(0.8)[kpc]	ecc(0.8)[kpc]
Aqu II	103 ⁺⁷ ₋₁₆	307 ⁺⁶³⁴ ₋₃₀₅	0.5 ⁺⁰ _{-0.31}	105 ⁺⁷ ₋₁₀	13425 ⁺¹⁰⁶¹⁵ ₋₁₃₂₉₇	0.98 ⁺⁰ _{-0.33}
Boo I	33 ⁺¹³ ₋₁₀	76 ⁺¹¹ ₋₈	0.4 ^{+0.11} _{-0.07}	45 ⁺⁹ ₋₁₂	115 ⁺⁷⁰ ₋₂₇	0.43 ^{+0.08} _{-0.03}
Boo II	39 ⁺² ₋₃	203 ⁺¹⁵⁵⁶ ₋₁₂₁	0.68 ^{+0.29} _{-0.29}	40 ⁺³ ₋₃	21309 ⁺²⁰⁰⁹⁷ ₋₂₀₉₂₀	1 ⁺⁰ _{-0.18}
CanVen I	75 ⁺³⁶ ₋₄₆	260 ⁺³²⁷ ₋₄₅	0.55 ^{+0.25} _{-0.13}	118 ⁺³⁵ ₋₆₃	371 ⁺⁶⁸²³ ₋₂₁₇	0.52 ^{+0.17} _{-0.14}
CanVen II	121 ⁺¹⁷ ₋₇₁	281 ⁺¹⁵³³⁷ ₋₁₇₈	0.4 ^{+0.13} _{-0.17}	137 ⁺¹⁶ ₋₅₅	1583 ⁺²⁸¹³ ₋₁₅₅₃	0.84 ^{+0.01} _{-0.29}
Car I	65 ⁺³² ₋₂₂	107 ⁺¹⁰ ₋₈	0.24 ^{+0.17} _{-0.16}	106 ⁺⁸ ₋₂₄	137 ⁺¹¹⁵ ₋₄₃	0.13 ^{+0.13} _{-0.09}
Car II	26 ⁺³ ₋₃	121 ⁺³² ₋₂₃	0.64 ^{+0.04} _{-0.03}	28 ⁺³ ₋₂	2156 ⁺⁹⁸⁹⁹ ₋₁₆₁	0.97 ^{+0.02} _{-0.06}
Car III	29 ⁺³ ₋₂	109 ⁺⁶⁶ ₋₄₀	0.58 ^{+0.11} _{-0.18}	29 ⁺³ ₋₂	6786 ⁺⁹⁴³⁰ ₋₆₄₉₆	0.99 ⁺⁰ _{-0.12}
ComBer I	44 ⁺⁵ ₋₆	71 ⁺⁴⁸ ₋₂₄	0.24 ^{+0.18} _{-0.12}	44 ⁺⁵ ₋₃	239 ⁺¹⁰⁹⁵ ₋₁₃₁	0.69 ^{+0.23} _{-0.13}
Cra I	31 ⁺³ ₋₃	145 ⁺⁷⁶⁹⁰ ₋₂₁	0.65 ^{+0.35} _{-0.46}	50 ⁺³ ₋₂₈	146 ⁺⁸⁰³⁶ ₋₁₀₇	0.49 ^{+0.13} _{-0.33}
Cra II	20 ⁺¹⁰ ₋₈	127 ⁺⁶ ₋₇	0.73 ^{+0.13} _{-0.06}	30 ⁺¹⁶ ₋₁₂	142 ⁺¹² ₋₁₉	0.65 ^{+0.13} _{-0.04}
Dra I	26 ⁺⁵ ₋₃	86 ⁺⁹ ₋₉	0.53 ^{+0.06} _{-0.05}	39 ⁺⁸ ₋₄	106 ⁺¹⁷ ₋₁₃	0.46 ^{+0.02} _{-0.06}
Dra II	22 ⁺³ ₋₄	80 ⁺⁴⁵ ₋₂₇	0.57 ^{+0.09} _{-0.09}	23 ⁺⁴ ₋₄	559 ⁺¹⁰⁶⁰⁰ ₋₄₁₂	0.92 ^{+0.06} _{-0.13}
Eri II	381 ⁺³⁸ ₋₄₄	95413 ⁺⁵⁵⁸⁰⁵ ₋₅₀₇₈₅	0.99 ⁺⁰ _{-0.01}	381 ⁺³⁸ ₋₄₄	97952 ⁺⁵⁵⁸⁰⁹ ₋₄₉₈₆₉	0.99 ⁺⁰ _{-0.01}
Frn I	88 ⁺⁵⁴ ₋₄₅	158 ⁺⁶⁹ ₋₂₀	0.28 ^{+0.2} _{-0.12}	134 ⁺²³ ₋₅₉	240 ⁺⁷²⁴ ₋₉₈	0.28 ^{+0.24} _{-0.11}
Gru I	69 ⁺²² ₋₂₈	476 ⁺¹⁵⁶⁵⁰ ₋₃₀₃	0.75 ^{+0.15} _{-0.11}	78 ⁺²⁰ ₋₂₅	17910 ⁺¹²⁵⁶⁹ ₋₁₆₆₆₁	0.99 ⁺⁰ _{-0.05}
Her I	54 ⁺³⁸ ₋₃₅	209 ⁺²⁹⁴⁵ ₋₆₂	0.59 ^{+0.23} _{-0.1}	71 ⁺⁴³ ₋₄₂	544 ⁺¹²⁹⁹² ₋₄₁₁	0.77 ^{+0.07} _{-0.12}
Hor I	61 ⁺¹⁹ ₋₂₅	84 ⁺⁴² ₋₁₀	0.16 ^{+0.12} _{-0.06}	77 ⁺⁸ ₋₁₆	152 ⁺³³⁵ ₋₇₂	0.33 ^{+0.31} _{-0.16}
Hyd II	95 ⁺¹² ₋₃₅	322 ⁺⁵⁴² ₋₃₁₉	0.55 ^{+0.24} _{-0.06}	132 ⁺¹³ ₋₃₄	8099 ⁺⁷²⁷⁷ ₋₇₉₃₉	0.97 ^{+0.18} _{-0.02}
Leo I	41 ⁺³⁹ ₋₂₅	510 ⁺¹⁰⁴⁵ ₋₁₁₅	0.85 ^{+0.11} _{-0.06}	58 ⁺⁶ ₋₄₇	1844 ⁺³²⁰¹ ₋₁₄₉₆	0.94 ^{+0.02} _{-0.03}
Leo II	96 ⁺¹⁷ ₋₆₅	238 ⁺¹⁶³⁹ ₋₃₇	0.43 ^{+0.36} _{-0.29}	185 ⁺¹⁹ ₋₈₆	249 ⁺⁶⁰⁵¹ ₋₁₇₉	0.15 ^{+0.06} _{-0.1}
Leo IV	155 ⁺¹⁰ ₋₁₄	16565 ⁺¹⁷⁷⁹¹ ₋₁₆₄₃₈	0.98 ⁺⁰ _{-0.44}	155 ⁺¹⁰ ₋₁₂	33628 ⁺²⁶⁰³⁰ ₋₂₉₀₃₀	0.99 ⁺⁰ _{-0.03}
Leo V	197 ⁺²⁰ ₋₂₃	32429 ⁺²²⁹⁴⁸ ₋₂₉₁₀₄	0.99 ⁺⁰ _{-0.04}	197 ⁺¹⁹ ₋₂₁	42469 ⁺²⁶³⁴⁴ ₋₂₆₁₂₂	0.99 ⁺⁰ _{-0.01}
Phe I	71 ⁺⁸ ₋₂₅	620 ⁺⁶¹⁰ ₋₅₉₃	0.79 ^{+0.01} _{-0.21}	107 ⁺¹⁰ ₋₂₆	1156 ⁺⁷⁶⁸ ₋₇₄₅	0.83 ^{+0.01} _{-0.02}
Pis II	177 ⁺²⁰ ₋₂₂	29187 ⁺²³⁵⁰⁴ ₋₂₆₈₃₁	0.99 ⁺⁰ _{-0.06}	178 ⁺¹⁹ ₋₂₁	40481 ⁺²⁹¹⁶⁰ ₋₂₆₅₆₉	0.99 ⁺⁰ _{-0.01}
Ret II	20 ⁺⁵ ₋₄	39 ⁺⁷ ₋₄	0.32 ^{+0.06} _{-0.02}	25 ⁺³ ₋₄	63 ⁺²⁸ ₋₁₆	0.43 ^{+0.09} _{-0.04}
Sgr I	15 ⁺³ ₋₃	36 ⁺¹⁰ ₋₈	0.42 ^{+0.04} _{-0.02}	16 ⁺² ₋₂	81 ⁺³¹ ₋₂₉	0.68 ^{+0.08} _{-0.08}
Scu I	51 ⁺⁸ ₋₇	100 ⁺⁸ ₋₈	0.33 ^{+0.05} _{-0.04}	69 ⁺⁶ ₋₇	164 ⁺⁴¹ ₋₂₅	0.4 ^{+0.06} _{-0.03}
Seg 1	16 ⁺⁶ ₋₆	36 ⁺¹⁰ ₋₆	0.37 ^{+0.1} _{-0.04}	20 ⁺⁵ ₋₆	56 ⁺⁴⁶ ₋₁₇	0.47 ^{+0.12} _{-0.04}
Seg 2	2 ⁺² ₋₁	34 ⁺² ₋₂	0.87 ^{+0.13} _{-0.24}	3 ⁺³ ₋₂	34 ⁺² ₋₂	0.83 ^{+0.17} _{-0.31}
Sext I	72 ⁺⁸ ₋₁₁	133 ⁺³² ₋₂₃	0.3 ^{+0.05} _{-0.02}	80 ⁺⁶ ₋₇	438 ⁺⁴⁵⁰ ₋₁₈₆	0.69 ^{+0.13} _{-0.14}
Tri II	17 ⁺² ₋₃	99 ⁺¹⁸ ₋₁₃	0.7 ^{+0.01} _{-0.01}	21 ⁺³ ₋₃	508 ⁺⁷⁷⁸ ₋₂₀₃	0.92 ^{+0.04} _{-0.03}
Tuc II	31 ⁺¹¹ ₋₉	111 ⁺⁶² ₋₂₉	0.57 ^{+0.04} _{-0.02}	36 ⁺⁹ ₋₉	391 ⁺⁴¹⁹⁵ ₋₂₁₅	0.83 ^{+0.15} _{-0.09}
Tuc III	3 ⁺¹ ₋₁	37 ⁺⁴ ₋₃	0.85 ^{+0.01} _{-0.02}	3 ⁺¹ ₋₁	55 ⁺⁷ ₋₆	0.88 ^{+0.01} _{-0.01}
UMaj I	101 ⁺⁷ ₋₁₂	192 ⁺³⁴⁹ ₋₈₇	0.31 ^{+0.34} _{-0.2}	101 ⁺⁶ ₋₇	1727 ⁺²¹²¹⁷ ₋₁₄₄₁	0.89 ^{+0.11} _{-0.42}
UMaj II	33 ⁺⁷ ₋₁₂	49 ⁺³⁶ ₋₁₃	0.19 ^{+0.1} _{-0.05}	36 ⁺⁵ ₋₈	108 ⁺²⁷¹ ₋₆₀	0.5 ^{+0.29} _{-0.21}
UMin I	28 ⁺⁶ ₋₄	85 ⁺⁶ ₋₆	0.5 ^{+0.06} _{-0.06}	44 ⁺⁸ ₋₇	100 ⁺¹¹ ₋₉	0.39 ^{+0.05} _{-0.03}
Wil I	13 ⁺¹⁰ ₋₅	43 ⁺⁷ ₋₇	0.53 ^{+0.2} _{-0.22}	20 ⁺¹⁵ ₋₉	43 ⁺¹² ₋₈	0.37 ^{+0.29} _{-0.23}
Hyd I	26 ⁺¹ ₋₁	257 ⁺⁹⁹³ ₋₁₄₅	0.82 ^{+0.12} _{-0.16}	26 ⁺¹ ₋₁	31184 ⁺¹⁰³⁹⁹ ₋₁₅₅₆₁	1 ⁺⁰ ₋₀

5.1. Apocenter Distances and Orbital Energies

Figure 2 allows us to see the number of galaxies that have orbits that will take them beyond the virial radius of the MW DM halo, i.e. those that have apocenters above the solid lines. Such satellites can be considered alongside the backsplash population of satellites that exist beyond the virial radius at $z=0$, but have been within the virial radius at earlier times (Balogh et al. 2000; Gill et al. 2005; Teyssier et al. 2012; Simpson et al. 2018). Assuming a high (low) mass halo implies that there are 37 (34) satellite galaxies within the virial radius at the present time, of which 9 (19) are “backsplashing” satellites in that their orbits

will take them beyond the virial radius. Of the 3 (6) dwarfs that are outside the virial radius at the present time, in the high (low) mass halo, 2 (4) are backsplashing. We can see in particular that a low mass halo would imply that the majority of the observed dwarfs are on orbits that pass in and out of the virial radius, whilst for a high mass halo a little more than a quarter of the galaxies are on such backsplashing orbits.

In Figure 1 we show how the newly measured 3D velocities of the satellites as a function of radius compare to the local escape velocity in the two MW potentials. The definition of whether a satellite is bound or not in an evolving cosmo-

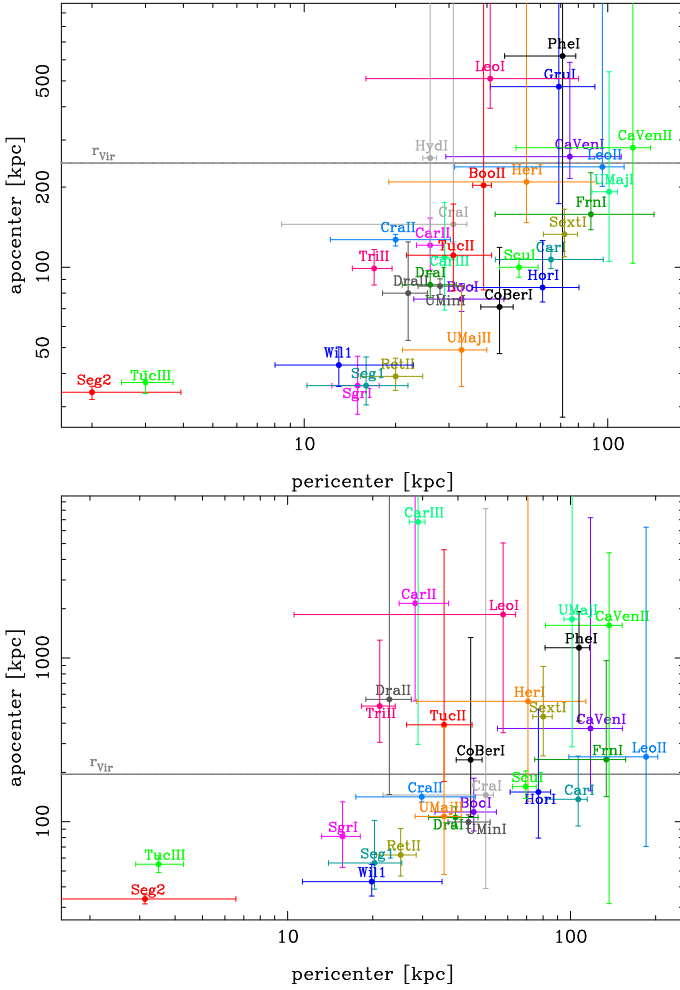


Fig. 2. Pericenter versus apocenter properties of the galaxies in the sample with 3D velocity errors <100 km/s, as indicated by the labels. The top panel plot shows the results for a MW DM halo of virial mass equal to $1.6 \times 10^{12} M_{\odot}$, and the lower panel for $0.8 \times 10^{12} M_{\odot}$. We also show typical virial radii in both plots. Some galaxies like Grus I are omitted in the lower plot because their very large apocenter would distort the plot.

logical context is complex, and the comparison to the curves should therefore be interpreted primarily in a relative sense. Boylan-Kolchin et al. (2013) addressed this topic in detail for the case of Leo I. That analysis was based on the proper motion of Leo I measured by HST, which is in good agreement with our Gaia DR2 value. They showed that the low-mass MW is actually ruled out at 95% confidence, since in such halos it is vanishingly rare in cosmological simulations to find subhalos at 261 kpc moving as fast as Leo I. By contrast, they showed that the high-mass Milky Way is the statistically preferred value. Given this result, our Figure 1 and large apocenter in Figure 2 shows that several other satellites (e.g. Car II, Car III, Grus I) have a combination of distance and velocity that will put them at odds with a low-mass MW. A few galaxies (Pis II, Leo V, Eri II) even have velocities that would make them hard to explain in a cosmological context for the high-mass MW model. In contrast Phoenix I seems bound at the first view, but as in case of other distant systems, detailed simulation of galaxy infall and our errors are necessary to confirm that.

5.2. Pericenter Distances and Tidal Influences

From Fig. 2 it can be noticed that Tuc III and Segue 2 are likely to reach within 10 kpc from the Milky Way center in both potentials and be confined within 50kpc, therefore highly likely to have been subject to strong tidal disturbances, as confirmed by the presence of a stream in Tucana III and predicted by Erkal et al. (2018). Also Willman 1, Reticulum II, Segue 1 have a very internal orbit, with a likely pericenter distance between 10 and 30 kpc; in the potential corresponding to the heavy dark matter halo their orbit would be confined within 50 kpc, while it could reach out to ~ 100 kpc for the lighter DM halo; the small pericentric distance does nonetheless make them candidates for having been significantly tidally perturbed.

As mentioned in the Introduction, elongations and/or isophote twists suggestive of tidal stretching of the stellar component have been observed in Carina I, Hercules and Boötes I. The errors on Hercules’s orbital properties are very large and prevent strong conclusions to be made; depending on the potential adopted, Boötes I orbit might get as close as to ~ 20 kpc from the MW center, while on the other hand Carina I is not expected to have come closer than ~ 50 kpc (within 1σ) for the heavy halo, while in the case of the light halo its orbit would be rather external. The observational findings of signs of likely tidal disturbance in Carina can be considered as robust as they have been detected in multiple studies in the literature adopting different methodologies (see e.g. Muñoz et al. 2006; Battaglia et al. 2012; McMonigal et al. 2014, and references in); their presence might then either suggest a preference for a heavy MW DM halo or that dwarf galaxies might experience strong tidal disturbance even on rather external orbits; we deem this latter hypothesis unlikely (see results from N-body simulations, e.g. Muñoz et al. 2008; Peñarrubia et al. 2008, for those simulated objects on similar orbits), but this is certainly an important aspect to be verified, since several of the MW dwarf galaxies are on more internal orbits than Carina (e.g. Draco, Ursa Minor, Boötes I, Crater II to mention a few) and could see their internal kinematic properties potentially affected. Alternatives could contemplate the possibility that the properties of Carina might have been affected by the Magellanic system: e.g. the recent infall of the Magellanic system might have modified Carina’s current orbital properties, making them therefore not representative of its past orbital history; however Carina shares with the LMC a very similar orientation of the time-average orbit (Gaia Collaboration et al. 2018b), while torques from the LMC would be expected to be maximal on systems on a perpendicular orbital plane; we speculate that Carina could have experienced a close encounter with the Magellanic Clouds and that perhaps these latter systems are responsible for inducing tidal disturbances.

While the perturbative influence of the LMC (Gómez et al. 2015) has not been included in the presented orbit calculations, it will be included in follow-up studies to assess the impact on the orbits of the classical and UFD satellites of the MW (Patel et al. in prep.).

In Fig. 4 we plot the distance from the Galactic center as a function of time for Crater II: in both the DM haloes for the *MWpotential14*, the best Crater II orbit is radial with an eccentricity of about 0.7 and can reach as close to the 20 kpc. That implies that the Hill radius of Crater II is at pericenter far smaller than Crater II half-light radius (see Figure 4, bottom panel), therefore confirming the prediction of Fattahi et al. (2018) and Sanders et al. (2018) that it is in process of tidal disruption. Our proper motion is in relatively good ($0.3/1.3\sigma$) agreement with the models by Sanders et al. (2018). Thus it seems likely

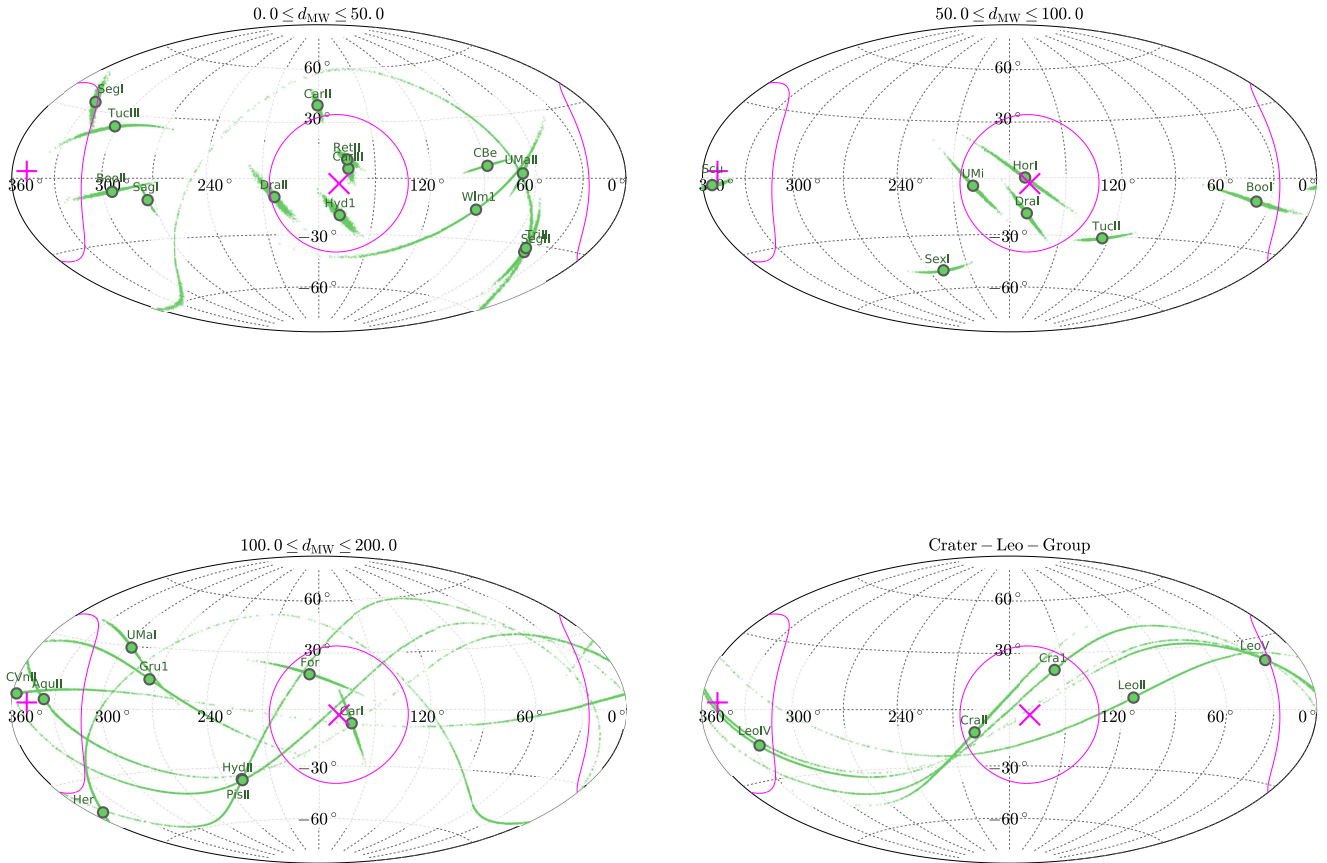


Fig. 3. All-sky view of orbital poles for the objects in the sample; the circles indicate the median of the 2000 Monte Carlo simulations while the small points around each object plot the orbital poles from the individual simulations. The magenta circles contain 10 per cent of the sky around the assumed VPOS pole, which is given as a “X” for the “co-orbiting” direction (orbital sense as most classical satellites, including the LMC and SMC), and a “+” for the opposite normal direction (“counter-orbiting”). Top panels: objects with Galactocentric distances between 0-50kpc (left) and 50-100kpc (right); bottom panels: objects with Galactocentric distances between 100-200kpc (left) and in the putative Crater-Leo group.

that Crater II fits in the standard Λ Cold Dark matter scenario but has lost the great majority of its mass to tidal interactions with the MW. There is still a small deviation which, when it gets more significant, might necessitate cored dark matter halos (Sanders et al. 2018) or deviation from General Relativity (McGaugh 2016).

As stated above, several other systems do share internal orbits such as Crater II and therefore the potential impact of tidal disturbances needs to be understood to properly interpret these systems’ structural and internal kinematic properties.

5.3. The Missing Satellite Problem

Figure 5 shows histograms of the ratio $f = (d_{GC} - r_{peri})/(r_{apo} - r_{peri})$. Both histograms have a peak at small value of f . This is more pronounced for the low-mass MW model, which based on the arguments in the preceding sections, we consider less plausible. Basic dynamics dictates that within their orbits, galaxies spend most of their time near apocenter, where the velocity is lower. Also, the number of galaxies at small pericenters ($\lesssim 20$

kpc) is reduced through tidal destruction. So if we had a *complete* sample of MW dwarfs, then the histograms would have to be increasing towards high f . By contrast, even for the high-mass MW, the observed histogram is flat at best. The corollary is that there must be a population of (ultra-faint) dwarf galaxies that are currently at apocenter, especially beyond ~ 100 kpc, that have yet to be discovered. This is relevant to the so-called “missing satellite” problem (see review in Kravtsov (2009)), as it affects the comparison of observed dwarf galaxy counts to subhalos found in hierarchical galaxy formation scenarios. Implications of this statement will be discussed in Patel et al. (in prep.).

5.4. Orbital Poles and Planar Alignments

Figure 3 shows the distribution of orbital poles for three distance bins (0 to 50, 50 to 100, and 100 to 200 kpc), as well as for the proposed members of the Crater-Leo Group (not included in the 100 to 200 kpc plot). The uncertainty in the direction of orbital poles is illustrated with point clouds based on the 2000 Monte Carlo simulations of the measurement uncertainties. The

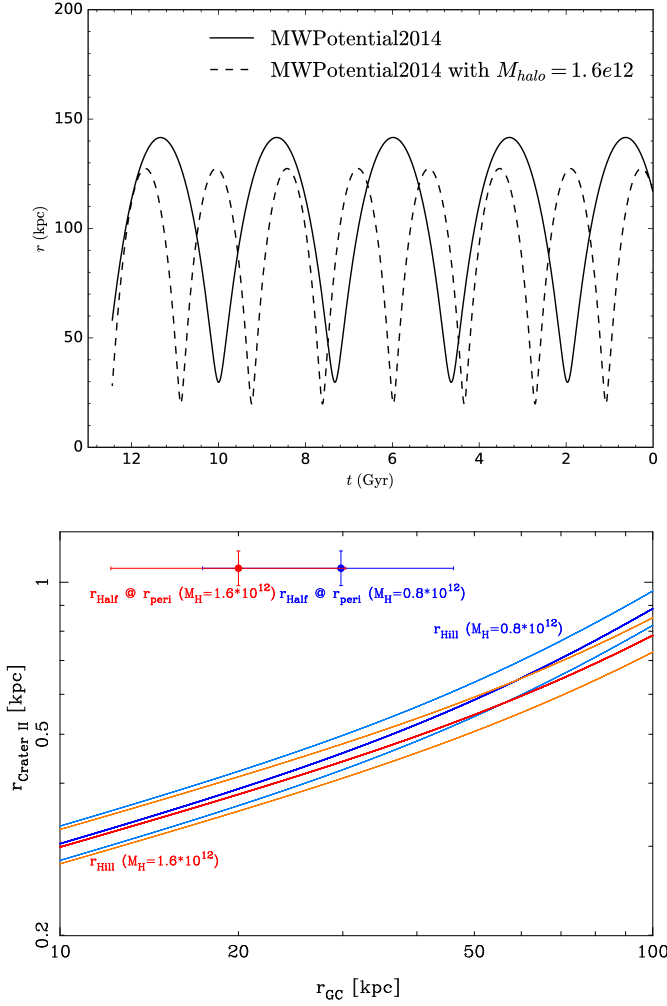


Fig. 4. Properties of Crater II. Top: Orbital integration for Crater II in the *MWpotential14* for the standard light halo (solid line) and the heavy DM halo (dashed line) plotted as the distance from the MW center as a function of time. Bottom: hill radius of a galaxy of the mass of Crater II (Caldwell et al. 2017) in two different MW potentials compared to the size and apocenter of Crater II.

magenta cross and plus sign gives the assumed normal direction to the VPOS, as used to predict the proper motions of satellites in Pawlowski & Kroupa (2013). The magenta circles of opening angle $\theta_{\text{inVPOS}} = 36.87^\circ$ denote areas of 10 per cent of the sphere around these directions. We consider orbital poles that lie within this region to orbit along the VPOS.

Based on the assumption that the satellite galaxies orbit along the VPOS, Pawlowski & Kroupa (2013); Pawlowski et al. (2015) predicted orbital poles for the satellite galaxies. We can now test how well these predictions are met. The predicted orbital pole direction is the direction along the great circle perpendicular to the satellite (as seen from the center of the Milky Way) which minimizes the angle to the assumed VPOS normal, which points to Galactic coordinates $(l, b) = (169.3^\circ, -2.8^\circ)$. The corresponding minimum angle between the VPOS normal and the pole of a satellite galaxy is θ^{pred} . The angle between the orbital pole based on our proper motions and the VPOS normal is θ^{obs} . The ratio between these gives a measure of how well an observed orbital pole agrees with its predicted direction. Figure 6 plots this ratio against a measure of the uncertainty in observed orbital

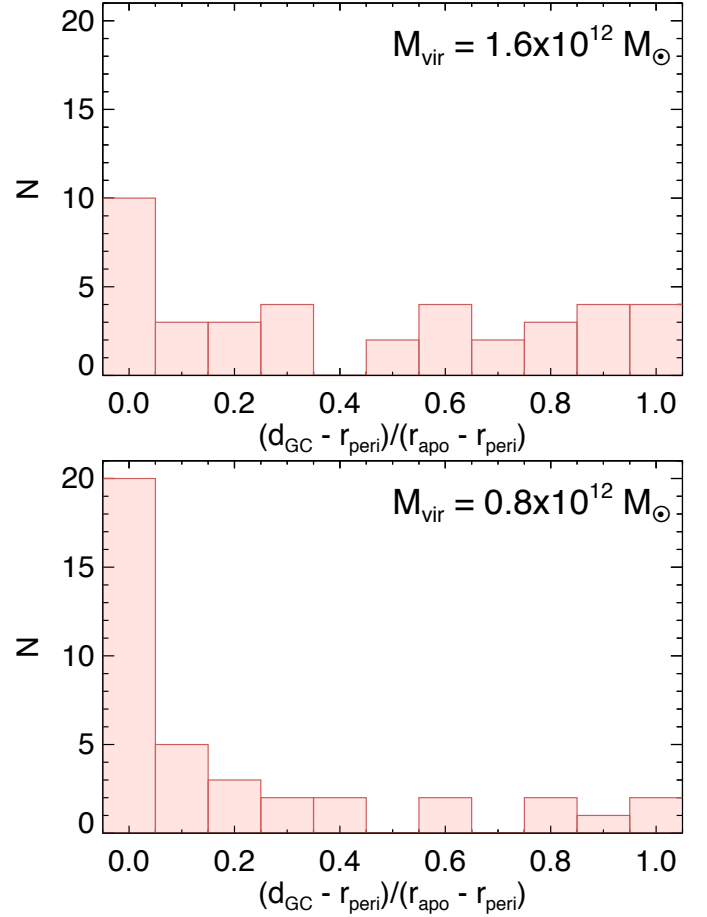


Fig. 5. This Figure shows histograms of the ratio $f = (d_{\text{GC}} - r_{\text{peri}}) / (r_{\text{apo}} - r_{\text{peri}})$, for both the high-mass and low-mass MW models (upper and lower panels, respectively). A galaxy on the left of each histogram is near pericenter, while a galaxy on the right of each histogram is near apocenter.

pole direction, Δ_{pole} . The latter is defined as the angle from the most-likely measured orbital pole of a satellite which contains 68 per cent of the orbital poles sampled from its measurement uncertainties. The ratio of observed to measured angle from the VPOS is typically large for objects with poorly constrained orbital pole directions ($\Delta_{\text{pole}} > 20^\circ$), but for those with smaller uncertainties the majority of objects (15 out of 22) agree to within a factor of two (dashed magenta line) with the predicted angle. Satellites co-orbiting with the majority of the classical satellite galaxies associated with the VPOS are plotted as green, upward triangle, whereas red downward triangles are used for counter-orbiting satellites. Satellites at larger distance are plotted with larger symbols.

Table 4 provides an overview of the predicted (θ^{pred}) and the measured (θ^{obs}) alignments of satellite orbital poles. The observed angle is given a negative sign if the measured orbital pole is counter-orbiting relative to the orbital direction of the majority of the classical satellite galaxies associated with the VPOS. For each satellite, we calculate the fraction $p_{(\text{inVPOS})}$ of Monte Carlo sample orbital pole directions which falls to within θ_{inVPOS} of the VPOS normal. For an orbital pole that is misaligned with the VPOS, this indicates whether there nevertheless is a chance that the pole might be aligned. Also given in the table is a measure of how strong the constraints of each satellite's pole are on its alignment with the VPOS direction. For the latter, we assume that the satellite's intrinsic orbital pole aligns perfectly with its

predicted direction. We then vary its orbital pole direction by sampling 2000 times from the measured uncertainties in orbital pole direction of this satellite. Since a satellite's orbital pole can not be better aligned than the predicted direction, any offset from this direction results in an increase of the angle with the VPOS normal. For each realisation, the angle to the VPOS normal is calculated. If it is larger than θ_{inVPOS} , we count this realisation as not aligned with the VPOS, even though we know that its intrinsic pole is perfectly aligned. The fraction of realisations counted this way gives an estimate of the probability $p_{>\text{VPOS}}$ to falsely find this satellite's orbital pole to be misaligned with the VPOS. It is compiled in column 5 of the table. We also count how often the angle to the VPOS exceeds $\theta_{\text{obs}}^{\text{obs}}$, the angle between the most-likely measured orbital pole and the VPOS normal. This gives an estimate of the probability $p_{>\text{obs}}$ to measure an intrinsically well aligned orbital pole as far away from the VPOS normal as observed. Since this method assumes intrinsically perfect alignments, the resulting probabilities should be seen as lower limits.

Overall, for 12 of the satellites the chance p_{inVPOS} to align with the VPOS to better than $\theta_{\text{pred}}^{\text{pred}}$ given our proper motion uncertainties is lower than 5 per cent. For the remaining 27 satellites, an alignment of their orbital pole with the VPOS is either found, or can not be rejected with high confidence. Six out of the 39 objects can not align with the VPOS because their predicted angle $\theta_{\text{pred}}^{\text{pred}}$ already exceeds θ_{inVPOS} : their spatial positions alone already place them outside of the VPOS plane orientation. A well known example is Sagittarius, which has an orbit almost perpendicular to the VPOS. The other satellites in this category are Hercules, Segue II, Triangulum II, Ursa Major II, and Wilman 1. Five of these counter-orbit relative to the VPOS, for a counter-orbiting fraction of $f_{\text{counter}} = \frac{5}{6} = 0.83$. Of the remaining 33 satellites for which an alignment is feasible, 16 have median orbital poles which align to within θ_{inVPOS} with the VPOS normal. The majority of these are well constrained to align with the VPOS, because most of their Monte Carlo sampled orbital poles also shows an alignment ($p_{\text{inVPOS}} > 0.5$). The two least certain alignments are Crater 1 and Leo IV, for which only 34 and 43 per cent of realisations fall to within θ_{inVPOS} of the VPOS normal, respectively. Of these 16 satellites with aligned orbital poles, only one has $p_{>\text{VPOS}} \geq 0.5$ (Crater 1), five have $0.4 \geq p_{>\text{VPOS}} \geq 0.17$, and the others have $p_{>\text{VPOS}} \gg 0.01$. This indicates that given the respective measurement uncertainties, the measured orbital poles are expected to be found within θ_{inVPOS} of the VPOS if the satellites orbit along the VPOS. It is also interesting to note that of these 16 satellites, five counter-orbit. These are Aqu II, CVn II, Leo IV, Seg I, and Sculptor, for which this was known previously). The remaining 11 satellites co-orbit, as do the LMC and SMC, so the counter-orbiting fraction is $f_{\text{counter}} = \frac{5}{16+2} = 0.28$.

The remaining 17 satellites have median orbital poles which do not align with the VPOS. Of these, nine have orbital pole directions that are too weakly constrained to be conclusive. These are CVn I, Eri II, Gru I, Hyd II, Leo I, Leo II, Leo V, Phe I, and Pis II. When the orbital pole directions are Monte Carlo sampled from the measured uncertainties, there about a one in three chance that the pole is aligned with the VPOS ($0.13 < p_{\text{inVPOS}} < 0.44$). These are thus consistent with aligning with the VPOS within their uncertainties. Even if their poles were intrinsically as well aligned as geometrically possible, due to the considerable uncertainty in their orbital pole directions their poles are expected to be found outside of θ_{inVPOS} with probabilities of $p_{>\text{VPOS}} = 37$ to 61 per cent. With $p_{(>\text{obs})} = 12.5$ to 55 per cent it is expected that the poles are as far or further from the VPOS as observed, except for Eri II and Gru I for which these probabilities are only 3 and 4 per cent, respectively. Two of the seven

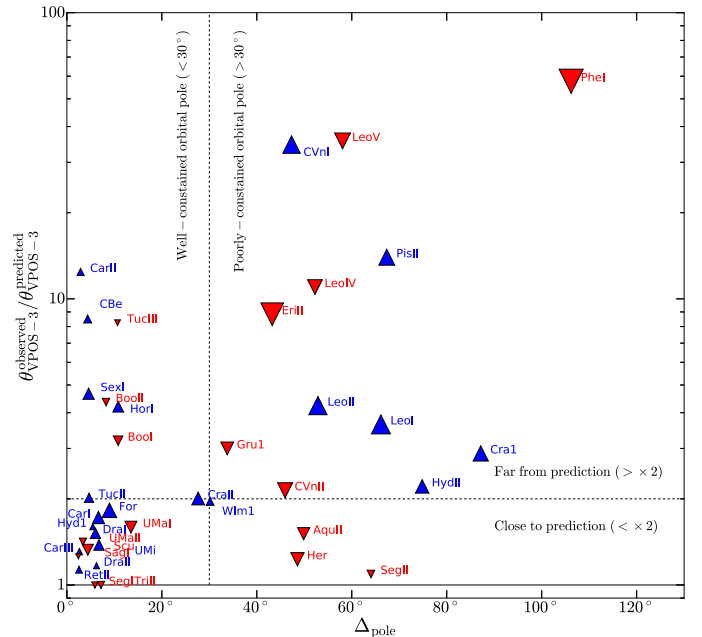


Fig. 6. Alignment with the VPOS, measured as the ratio between the measured (θ_{obs}) and the predicted (θ_{pred}) angular offset of an orbital pole from the VPOS, plotted against the uncertainty (Δ_{pole}) in the direction of the orbital pole. Blue, upward triangles are co-orbiting relative to the majority of classical satellites including the LMC, red downward triangles are counter-orbiting. Symbol size increases with Galactocentric distance.

are more likely counter-orbiting, the remaining five more likely co-orbiting relative to the VPOS, so the counter-orbiting fraction is $f_{\text{counter}} = \frac{2}{7} = 0.29$.

Of the remaining eight satellites which have orbital poles that are misaligned with the VPOS normal, two are consistent with aligning to within θ_{inVPOS} at a 7 and 10 per cent level (Bootes I and Tucana III, respectively). However, it is basically impossible that these align as well as geometrically possible with the VPOS, because $p_{>\text{VPOS}} = 0$. This means that if these satellites orbit in the VPOS, then their poles can not be as quite close to the VPOS normal geometrically possible. Both satellites are most-likely counter-orbiting.

Thus, only six of the satellites have orbital poles that are firmly and conclusively misaligned with the VPOS even though they could have had aligned poles. These are Boo II, Car II, CBe, Sex I, Tuc II, and UMa I. They all have well constrained orbital pole directions $p_{\text{inVPOS}} \leq 0.01$ and $p_{>\text{obs}} = 0$ thus are not orbiting along the plane defined by the VPOS. Two of the six are most-likely counter-orbiting ($f_{\text{counter}} = 0.33$). For a more in-depth analysis in regard to the VPOS, we refer the reader to Pawlowski et al. (in prep.).

5.5. Group Infall

The orbital pole of the LMC is similar to the direction of the VPOS normal. Therefore our proper motion measurements suggest that several of the dwarf galaxies in the sample that have orbital poles falling within 10% of the sky around the assumed VPOS normal in the co-rotating assumption might be associated to the LMC. The association of MW dwarf galaxies to the Mag-

Table 4. Alignment with the VPOS. Column 1 gives the name of the satellite, col. 2 the angle between the predicted orbital pole and the VPOS normal, col. 3 the angle between the median measured orbital pole and the VPOS normal, col. 4 the fraction of Monte Carlo realizations that have an orbital pole aligned with the VPOS to within the 10 per cent circles, col. 5 the probability to falsely find an intrinsically perfectly aligned orbital pole outside of this area given the measurement uncertainties, and col. 6 the probability to find an orbital pole at least as far inclined from the VPOS as the median measured orbital pole.

Name	$\theta^{\text{pred}} [^\circ]$	$\theta^{\text{obs}} [^\circ]$	$f_{(\text{inVPOS})}$	$P(>\text{VPOS})$	$P(>\text{obs})$
AquII	7.8	-11.7	0.555	0.433	0.858
BooI	16.1	-51.3	0.069	0.003	0.000
BooII	12.8	-55.7	0.012	0.000	0.000
CVnI	1.5	51.8	0.388	0.443	0.257
CVnII	4.2	-9.0	0.593	0.401	0.854
CarI	4.7	8.0	1.000	0.000	0.331
CarII	3.5	43.4	0.011	0.000	0.000
CarIII	7.1	9.3	1.000	0.000	0.021
CBe	9.6	81.5	0.000	0.000	0.000
CraI	9.6	27.6	0.338	0.548	0.682
CraII	15.2	30.6	0.584	0.216	0.340
DraI	10.4	15.8	1.000	0.000	0.051
DraII	29.9	34.9	0.710	0.001	0.004
EriII	9.3	-82.6	0.211	0.366	0.028
For	14.6	26.6	0.899	0.001	0.016
GruI	24.9	-74.7	0.133	0.411	0.044
Her	37.7	-46.3	0.000	1.000	0.487
HorI	1.0	4.1	0.996	0.002	0.698
HydII	28.9	63.9	0.165	0.611	0.206
LeoI	20.4	74.3	0.242	0.503	0.124
LeoII	13.4	56.6	0.306	0.445	0.239
LeoIV	2.7	-29.4	0.433	0.410	0.510
LeoV	1.1	-39.1	0.430	0.582	0.553
PheI	0.8	-48.4	0.437	0.519	0.394
PisII	4.6	63.9	0.339	0.539	0.234
RetII	11.9	13.5	1.000	0.000	0.009
SagI	60.2	-75.9	0.000	1.000	0.000
Scu	5.0	-6.6	1.000	0.000	0.328
SegI	36.1	-36.0	0.730	0.168	1.000
SegII	58.7	-64.1	0.000	1.000	0.597
SexI	14.7	68.6	0.000	0.000	0.000
TriII	64.5	-64.5	0.000	1.000	0.850
TucII	25.3	51.0	0.000	0.000	0.000
TucIII	6.1	-50.5	0.095	0.000	0.000
UMaI	36.0	-57.3	0.001	0.526	0.000
UMaII	55.4	-78.4	0.000	1.000	0.000
UMi	21.7	30.0	0.902	0.001	0.004
WlmI	39.1	76.6	0.000	1.000	0.003
HydI	10.5	16.7	1.000	0.000	0.013

ellanic system will be the subject of a future work (Kallivayalil in prep.).

Mainly on the basis of the objects position on the sky and heliocentric distance, Torrealba et al. (2016a) argued that Crater 1, Crater II, Leo II, Leo IV and Leo V might have once formed part of a group accreted by the MW. Even though the errors on the orbital pole determinations are large, our analysis suggests such a prior physical association of all five objects together is unlikely. Given the large measurement uncertainties, the poles of Leo IV and V are probably rather unconstrained. Also Crater 1 has a

large uncertainty. In contrast the poles of Crater II and Leo II are better constrained and they do not overlap well. In addition, the preferred pericenter of these two objects differs by about 50 kpc.

Similarly, but with lower significance, Crater 1 has also different orbital characteristics than Leo II. Thus, we cannot exclude the possibility that there are two groups, one including Crater 1 and II, and the other one with Leo II and possibly the two other Leo galaxies, but we deem it unlikely that all the five objects came together as one group. Since, however the HST proper motion measurements places Leo II's orbital pole in the VPOS direction (Sohn et al. 2013; Piatek et al. 2016; Pawlowski et al. 2017), it might be possible that none of the measurement of Leo II is accurate enough and that further studies with either HST or Gaia are necessary.

6. Summary and conclusions

We derive systemic proper motions for all dwarf galaxies or galaxy candidates within 420kpc using Gaia DR2 proper motions, for which literature spectroscopic members are available. Our proper motion determinations for the classical MW dwarf spheroidal galaxies are in very good agreement (generally within 1σ , at most within 2σ) with the determinations by Gaia Collaboration et al. (2018b).

We derive the implied Galactocentric velocities, and calculate orbits in canonical MW halo potentials of "low" ($0.8 \times 10^{12} M_\odot$) and "high" mass ($1.6 \times 10^{12} M_\odot$). Comparison of the distributions of orbital apocenters and 3D velocities to the halo virial radius and escape velocity, respectively, suggests that the satellite kinematics are best explained in the high-mass halo. Relevant to the missing satellite problem, the fact that fewer galaxies are observed to be near apocenter than near pericenter implies that there must be a population of distant dwarf galaxies yet to be discovered.

Our analysis suggests that several UFDs, as well as a couple of classical MW dSphs such as Draco and UMi, have internal orbits with pericenter distances that bring them dangerously close to the internal regions of our Galaxy, at risk of being strongly tidally affected. The "feeble giant" Crater II is found to be on a $\sim 1:6$ peri-to-apocentric distance orbit (with a ~ 0.7 eccentricity) and a small pericentric distance, of approximately 20-30kpc, depending on the assumed MW DM halo mass. Our proper motion determination is in agreement with the predictions by Sanders et al. (2018) which see Crater II as embedded in a Λ CDM DM halo - possibly weakly cusped - which has experienced very strong mass loss due to tides. Since several other objects in the sample share with Crater II similar, or more extreme, internal orbits, it appears crucial to address in more detail the impact that tidal disturbances might have had in the structural and internal kinematic properties of these galaxies.

Of the 22 satellites for which we can draw conclusions, 16 are orbiting along the plane of satellites (VPOS, not counting the well aligned LMC and SMC) and 6 are not. These findings suggest that a majority of the MW satellites for which we have measured proper motions orbits along the VPOS, but that not all satellites participate in coherent motion along this structure. This is in line with an analysis based solely on the spatial distribution of satellite galaxies, which found that up to half of the MW satellites might be drawn from an isotropic distribution in addition to satellites drawn from a planar distribution (Pawlowski 2016), as well as with the satellite plane around Andromeda which consists of about half of the M31 satellites (Ibata et al. 2013).

The distribution of orbital poles does not appear to confirm the hypothesis that Crater 1, Crater II, Leo II, Leo IV and Leo V

were all accreted by the MW as part of the same galaxy group; although the errors are large and we cannot exclude an association between Crater 1 & Crater II or Leo II with Leo IV & Leo V, it seems unlikely that these objects are all associated to each other.

Finally, we note that we just use part of the power of Gaia DR2 for the determination of systemic proper motions of dwarf galaxies and this has already led to constraining proper motions for dozens of galaxies. We expect that in some cases adding stars without existing spectroscopic measurements should improve the precision. Since the precision in proper motion determinations grows with the 1.5 power of the time-baseline (and systematics also, when they are not based on a moving reference frame) we expect that the proper motions of Gaia should be a factor 4.5 more accurate after the nominal mission and possibly a factor 12 after the extended mission. This would enable to measure systemic proper motions for essentially all galaxies in the sample with the best precision now possible for very few galaxies. For example, even the motion of Phoenix I could be measured to about 4 km/s precision, as good as the current tangential motion measurement of Draco, the second best current measurement of HST up till now.

Acknowledgements. This work has made use of data from the European Space Agency (ESA) mission *Gaia* (<https://www.cosmos.esa.int/gaia>), processed by the *Gaia* Data Processing and Analysis Consortium (DPAC, <https://www.cosmos.esa.int/web/gaia/dpac/consortium>). Funding for the DPAC has been provided by national institutions, in particular the institutions participating in the *Gaia* Multilateral Agreement. G.B. gratefully acknowledges financial support by the Spanish Ministry of Economy and Competitiveness (MINECO) under the Ramon y Cajal Programme (RYC-2012-11537) and the grant AYA2014-56795-P. MSP acknowledges that support for this work was provided by NASA through Hubble Fellowship Grant #HST-HF2-51379.001-A awarded by the Space Telescope Science Institute, which is operated by the Association of Universities for Research in Astronomy, Inc., for NASA, under contract NAS5-26555. NK is supported by the NSF CAREER award 1455260. This project is part of the HSTPROMO (High-resolution Space Telescope PROper MOTion) Collaboration², a set of projects aimed at improving our dynamical understanding of stars, clusters and galaxies in the nearby Universe through measurement and interpretation of proper motions from HST, Gaia, and other space observatories. We thank the collaboration members for the sharing of their ideas and software. We thank Josh Simon to provide the catalogs of Simon & Geha (2007).

References

Adén, D., Feltzing, S., Koch, A., et al. 2009, *A&A*, 506, 1147
 Balogh, M. L., Navarro, J. F., & Morris, S. L. 2000, *ApJ*, 540, 113
 Battaglia, G., Irwin, M., Tolstoy, E., de Boer, T., & Mateo, M. 2012, *ApJ*, 761, L31
 Battaglia, G. & Starkenburg, E. 2012, *A&A*, 539, A123
 Battaglia, G., Tolstoy, E., Helmi, A., et al. 2011, *MNRAS*, 411, 1013
 Battaglia, G., Tolstoy, E., Helmi, A., et al. 2006, *A&A*, 459, 423
 Bechtol, K., Drlica-Wagner, A., Balbinot, E., et al. 2015, *ApJ*, 807, 50
 Bland-Hawthorn, J. & Gerhard, O. 2016, *ARA&A*, 54, 529
 Bovy, J. 2015, *ApJS*, 216, 29
 Boylan-Kolchin, M., Bullock, J. S., Sohn, S. T., Besla, G., & van der Marel, R. P. 2013, *ApJ*, 768, 140
 Caldwell, N., Walker, M. G., Mateo, M., et al. 2017, *ApJ*, 839, 20
 Cifuentes, L., Battaglia, G., Irwin, M., et al. 2018, *A&A*, 609, A53
 Erkal, D., Li, T. S., Koposov, S. E., et al. 2018, *ArXiv e-prints* [arXiv:1804.07762]
 Fattahi, A., Navarro, J. F., Frenk, C. S., et al. 2018, *MNRAS*, 476, 3816
 Fritz, T. K., Linden, S. T., Zivick, P., et al. 2017a, *ApJ*, 840, 30
 Fritz, T. K., Lokken, M., Kallivayalil, N., et al. 2017b, *ArXiv e-prints* [arXiv:1711.09097]
 Gaia Collaboration, Brown, A. G. A., Vallenari, A., et al. 2018a, *ArXiv e-prints* [arXiv:1804.09365]

Gaia Collaboration, Helmi, A., van Leeuwen, F., et al. 2018b, *ArXiv e-prints* [arXiv:1804.09381]
 Gaia Collaboration, Prusti, T., de Bruijne, J. H. J., et al. 2016, *A&A*, 595, A1
 Gill, S. P. D., Knebe, A., & Gibson, B. K. 2005, *MNRAS*, 356, 1327
 Gómez, F. A., Besla, G., Carpintero, D. D., et al. 2015, *ApJ*, 802, 128
 Grillmair, C. J. 2009, *ApJ*, 693, 1118
 Ibata, R. A., Lewis, G. F., Conn, A. R., et al. 2013, *Nature*, 493, 62
 Kacharov, N., Battaglia, G., Rejkuba, M., et al. 2017, *MNRAS*, 466, 2006
 Kazantzidis, S., Mayer, L., Callegari, S., Dotti, M., & Moustakas, L. A. 2017, *ApJ*, 836, L13
 Kim, D., Jerjen, H., Geha, M., et al. 2016, *ApJ*, 833, 16
 Kirby, E. N., Boylan-Kolchin, M., Cohen, J. G., et al. 2013, *ApJ*, 770, 16
 Kirby, E. N., Cohen, J. G., Simon, J. D., et al. 2017, *ApJ*, 838, 83
 Kirby, E. N., Guhathakurta, P., Simon, J. D., et al. 2010, *ApJS*, 191, 352
 Kirby, E. N., Simon, J. D., & Cohen, J. G. 2015, *ApJ*, 810, 56
 Koch, A., Wilkinson, M. I., Kley, J. T., et al. 2009, *ApJ*, 690, 453
 Koposov, S. E., Belokurov, V., Torrealba, G., & Evans, N. W. 2015a, *ApJ*, 805, 130
 Koposov, S. E., Casey, A. R., Belokurov, V., et al. 2015b, *ApJ*, 811, 62
 Koposov, S. E., Gilmore, G., Walker, M. G., et al. 2011, *ApJ*, 736, 146
 Koposov, S. E., Walker, M. G., Belokurov, V., et al. 2018, *ArXiv e-prints* [arXiv:1804.06430]
 Kravtsov, A. 2009, in *Astronomical Society of the Pacific Conference Series*, Vol. 419, *Galaxy Evolution: Emerging Insights and Future Challenges*, ed. S. Jogee, I. Marinova, L. Hao, & G. A. Blanc, 283
 Li, T. S., Simon, J. D., Drlica-Wagner, A., et al. 2017, *ApJ*, 838, 8
 Li, T. S., Simon, J. D., Kuehn, K., et al. 2018a, *ArXiv e-prints* [arXiv:1804.07761]
 Li, T. S., Simon, J. D., Pace, A. B., et al. 2018b, *ArXiv e-prints* [arXiv:1802.06810]
 Łokas, E. L. 2009, *MNRAS*, 394, L102
 Łokas, E. L., Klimentowski, J., Kazantzidis, S., & Mayer, L. 2008, *MNRAS*, 390, 625
 Majewski, S. R., Schiavon, R. P., Frinchaboy, P. M., et al. 2017, *AJ*, 154, 94
 Martin, N. F., Geha, M., Ibata, R. A., et al. 2016, *MNRAS*, 458, L59
 Martin, N. F., Ibata, R. A., Chapman, S. C., Irwin, M., & Lewis, G. F. 2007, *MNRAS*, 380, 281
 Mateo, M., Olszewski, E. W., & Walker, M. G. 2008, *ApJ*, 675, 201
 Mayer, L., Governato, F., Colpi, M., et al. 2001, *ApJ*, 559, 754
 Mayer, L., Mastroiello, C., Wadsley, J., Stadel, J., & Moore, B. 2006, *MNRAS*, 369, 1021
 McGaugh, S. S. 2016, *ApJ*, 832, L8
 McMonigal, B., Bate, N. F., Lewis, G. F., et al. 2014, *MNRAS*, 444, 3139
 Muñoz, R. R., Majewski, S. R., & Johnston, K. V. 2008, *ApJ*, 679, 346
 Muñoz, R. R., Majewski, S. R., Zaggia, S., et al. 2006, *ApJ*, 649, 201
 Navarro, J. F., Frenk, C. S., & White, S. D. M. 1996, *ApJ*, 462, 563
 Pawlowski, M. S. 2016, *MNRAS*, 456, 448
 Pawlowski, M. S., Ibata, R. A., & Bullock, J. S. 2017, *ApJ*, 850, 132
 Pawlowski, M. S. & Kroupa, P. 2013, *MNRAS*, 435, 2116
 Pawlowski, M. S., McGaugh, S. S., & Jerjen, H. 2015, *MNRAS*, 453, 1047
 Pawlowski, M. S., Pflamm-Altenburg, J., & Kroupa, P. 2012, *MNRAS*, 423, 1109
 Peñarrubia, J., Navarro, J. F., & McConnachie, A. W. 2008, *ApJ*, 673, 226
 Piatek, S., Pryor, C., & Olszewski, E. W. 2016, *AJ*, 152, 166
 Revaz, Y. & Jablonka, P. 2018, *ArXiv e-prints* [arXiv:1801.06222]
 Roderick, T. A., Jerjen, H., Mackey, A. D., & Da Costa, G. S. 2015, *ApJ*, 804, 134
 Roderick, T. A., Mackey, A. D., Jerjen, H., & Da Costa, G. S. 2016, *MNRAS*, 461, 3702
 Sales, L. V., Helmi, A., & Battaglia, G. 2010, *Advances in Astronomy*, 2010, 194345
 Sanders, J. L., Evans, N. W., & Dehnen, W. 2018, *ArXiv e-prints* [arXiv:1802.09537]
 Simon, J. D. 2018, *ArXiv e-prints* [arXiv:1804.10230]
 Simon, J. D., Drlica-Wagner, A., Li, T. S., et al. 2015, *ApJ*, 808, 95
 Simon, J. D. & Geha, M. 2007, *ApJ*, 670, 313
 Simon, J. D., Geha, M., Minor, Q. E., et al. 2011, *ApJ*, 733, 46
 Simon, J. D., Li, T. S., Drlica-Wagner, A., et al. 2017, *ApJ*, 838, 11
 Simpson, C. M., Grand, R. J. J., Gómez, F. A., et al. 2018, *MNRAS* [arXiv:1705.03018]
 Sohn, S. T., Besla, G., van der Marel, R. P., et al. 2013, *ApJ*, 768, 139
 Spencer, M. E., Mateo, M., Walker, M. G., et al. 2017, *AJ*, 153, 254
 Teyssier, M., Johnston, K. V., & Kuhlen, M. 2012, *MNRAS*, 426, 1808
 Tolstoy, E., Irwin, M. J., Helmi, A., et al. 2004, *ApJ*, 617, L119
 Torrealba, G., Koposov, S. E., Belokurov, V., & Irwin, M. 2016a, *MNRAS*, 459, 2370
 Torrealba, G., Koposov, S. E., Belokurov, V., et al. 2016b, *MNRAS*, 463, 712
 Voggel, K., Hilker, M., Baumgardt, H., et al. 2016, *MNRAS*, 460, 3384
 Walker, M. G., Belokurov, V., Evans, N. W., et al. 2009a, *ApJ*, 694, L144
 Walker, M. G., Mateo, M., & Olszewski, E. W. 2009b, *AJ*, 137, 3100
 Walker, M. G., Mateo, M., Olszewski, E. W., et al. 2016, *ApJ*, 819, 53
 Walker, M. G., Olszewski, E. W., & Mateo, M. 2015, *MNRAS*, 448, 2717

² <http://www.stsci.edu/marel/hstpromo.html>